

WaveFuse: A Unified Deep Framework for Image Fusion with Discrete Wavelet Transform

Shaolei Liu, Manning Wang[†], Zhijian Song[†],

Abstract—We propose an unsupervised image fusion architecture for multiple application scenarios based on the combination of multi-scale discrete wavelet transform through regional energy and deep learning. To our best knowledge, this is the first time that a conventional image fusion method has been combined with deep learning for feature maps fusion. The useful information of feature maps can be utilized adequately through multi-scale discrete wavelet transform in our proposed method. Compared with other state-of-the-art fusion methods, the proposed algorithm exhibits better fusion performance in both subjective and objective evaluation. Moreover, it's worth mentioning that comparable fusion performance trained in COCO dataset can be obtained by training with a much smaller dataset with only hundreds of images chosen randomly from COCO. Hence, the training time is shortened substantially, leading to the improvement of the model's performance both in practicality and training efficiency.

Index Terms—Multi-scene image fusion, unsupervised learning, deep learning, discrete wavelet transform, regional energy

I. INTRODUCTION

IMAGE fusion is the technique of integrating complementary information from multiple images obtained by different sensors of the same scene, so as to improve the richness of the information contained in one image [1]. Image fusion can compensate for the limitation of single imaging sensors, and this technique has developed rapidly in recent years because of the wide availability of different kinds of imaging devices [1]–[3]. For example, in medical imaging applications, images of different modalities can be fused to achieve more reliable and precise medical diagnosis [4]. In military surveillance applications, image fusion integrates information from different electromagnetic spectrums (such as visible and infrared bands) to achieve night vision [2]. The process of image fusion can be divided into three steps. First, feature maps are extracted from the original source images. Then, the feature maps are fused by specific fusion rules. Finally, the fused image is reconstructed from the fused feature map. Therefore, the extraction of feature maps and the selection of fusion rules are the two key factors determining the quality of the fused image [5], and most studies focus on proposing new methods based on these two factors.

Before the overwhelming application of deep learning in image processing, many conventional approaches were used

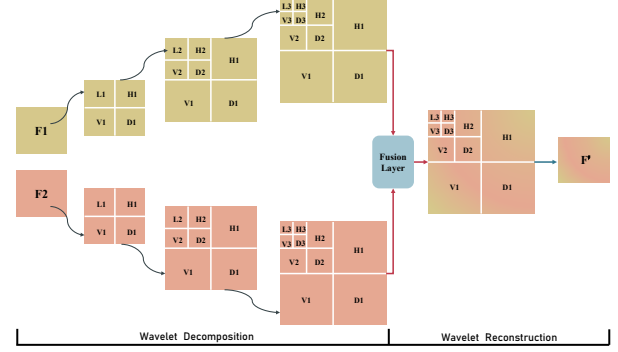


Fig. 1. Fusion process of feature maps by multi-scale discrete wavelet transform, where the wavelet decomposition layer is set as three for example.

in feature extraction for image fusion, which can be divided into two categories: transform domain algorithms and spatial domain algorithms [2]. In transform domain algorithms, the source images are transformed to a specific transform domain, such as the frequency domain, where the feature maps are represented by the decomposition coefficients of the specific transform domain. In feature maps fusion, max-rule and averaging are commonly used for high and low frequency bands, respectively, and then the fused image is reconstructed by the inverse transform from the fused feature maps [6]–[10]. Unlike transform domain algorithms, spatial domain algorithms employ the original pixel of source images as feature maps and directly calculate the weighted average of the source images to obtain the final fused image without dedicated feature maps extraction, where the weights are selected according to image blocks [11] or gradient information [12]. Consequently, the conventional approaches can be regarded as designing some hand-crafted filters to process the source images, and it is difficult for them to adapt to images of different scenes or parts with different visual cues in one image.

Nowadays, deep learning has been the state-of-the-art solution in most tasks in the fields of image processing and computer vision, such as image segmentation [13], classification [14] and object detection [15]. Recently, deep learning has also been used in image fusion and achieved higher quality than conventional methods. For example, CNN can be used to automatically extract useful features and can learn the direct mapping from source images to feature maps. In recent image fusion research based on deep learning [3]–[5], [16]–[19], fusion using learned features through CNN achieved higher quality than conventional fusion approaches. According to the different fusion framework utilized, deep learning based

S. Liu, M. Wang and Z. Song are with Digital Medical Research Center, School of Basic Medical Science, Fudan University, Shanghai 200032, China, and also with the Shanghai Key Laboratory of Medical Image Computing and Computer Assisted Intervention, Shanghai 200032, China(email: liushaolei@fudan.edu.cn; zjsong@fudan.edu.cn; mnwang@fudan.edu.cn).

[†] Corresponding authors

methods can be divided into the following three categories: CNN based methods [5], [19], [20], encoder-decoder based methods [4], [16], [17] and generative adversarial network (GAN) based methods [21]. CNN based methods merely apply several convolutional layers to obtain the weight map for source images. Encoder-decoder based methods introduce encoder-decoder architecture to extract deep features, and the deep features are fused by weighted average or concatenation. Furthermore, GAN based methods leverage conditional GAN to generate the fused image, where the concatenated source images are directly input to the generator. In these studies, the feature maps obtained through deep learning are usually simply fused by weighted averaging, and we will show that this is not optimal. More importantly, the neural networks used in these studies [4], [5], [16], [17], [19] usually need to be trained on large image dataset, which is time consuming.

In this paper, we propose an image fusion algorithm by combining the deep learning based approaches with conventional transform domain based approaches. Concretely, we first train an encoder-decoder network and extract feature maps from the source images by the encoder. In order to make the best use of the information of feature maps, discrete wavelet transform (DWT) is then utilized to transform the feature maps into the wavelet domain, and adaptive fusion rules are used at low and high frequencies, where the fusion process of feature maps by DWT is depicted in Fig. 1. Finally, inverse wavelet transform is used to reconstruct the fused feature map, which is decoded by the decoder to obtain the final fused image. Experiments show that with the additional processing of the feature maps by DWT, the quality of the fused image is remarkably improved. To the best of our knowledge, this is the first time to adopt conventional transform domain approaches to fuse the feature maps obtained from deep learning approaches.

The main contributions are summarized as follows:

- (1) A generalized and effective unsupervised image fusion framework is proposed based on the combination of multi-scale discrete wavelet transform and deep learning.
- (2) With multi-scale decomposition in DWT, the useful information of feature maps can be fully utilized. Moreover, a region-based fusion rule is adopted to capture more detail information. Extensive experiments demonstrate the superiority of our network over the state-of-the-art fusion methods.
- (3) Our network can be trained in a smaller dataset with low computational cost to achieve comparable fusion performance compared with existing deep learning based methods trained on full COCO dataset. Our experiments show that the quality of the fused images and the training efficiency are improved sharply.

Our paper is structured as follows. In Section II, we briefly review related works. In Section III, the proposed network and fusion rule are introduced in detail. The Section IV introduces the experimental results and analysis. In the last section, we give the conclusions of our paper.

II. RELATED WORKS

A. Conventional Image Fusion Methods

Conventional image fusion methods, including spatial domain and transform domain methods, have been studied for

multiple image fusion tasks. In spatial domain methods, image fusion is performed by weighted averaging of the source images according to image blocks [11] or gradient information [12]. In transform domain methods, the source images are first transformed into a series of frequency bands in a specific transformed domain, and then an appropriate fusion rule is used to fuse the different frequency bands. Finally, the fused frequency bands are reverse-transformed to obtain the final fused image. Multi-scale transform are widely used for the transform domain image fusion, such as Laplacian pyramid (LP) [9], discrete wavelet transform (DWT) [6], curvelet transform (CVT) [7] and non-subsampled contourlet transform (NSCT) [8], [10]. Max-rule and averaging are commonly applied to fuse the high and low frequency bands, respectively in the transform domain. However, due to the sensitivity to high frequency components, the brightness and color distortions are unavoidable. To resolve the limitations, Liu et al. [22] proposed a fusion method based on convolutional sparse representation (CSR), where multi-scale and multi-layer features are employed to reconstruct the fused output. Although conventional image fusion methods have achieved promising fusion performance, the limited choices of human-designed transformation and fusion rules hinder further improvement.

B. Deep Learning Based Image Fusion Methods

Compared to the conventional fusion methods, deep learning based methods achieve higher image quality owing to its powerful capacity of feature extraction. According to the fusion framework used, deep learning based methods can be further classified into three categories: CNN-based methods, encoder-decoder based methods and GAN-based methods.

1) *CNN Based Methods*: CNN was applied to an image fusion task for the first time in Liu et al. [5]. This method directly learns the mapping from the source image to the focus map through deep learning. By virtue of the CNN model, the selection of feature maps and fusion rules can be done simultaneously. Following [5], Liu et al. [20] extended the CNN model to fuse multi-modal medical images. In [20], CNNs are used to generate a weight map representing the pixel activity information of the source images, and the fusion process is performed in a multi-scale way through the image pyramid, where the fused results are more consistent with human visual perception. In addition, the strategy based on local similarity is introduced to adjust the fusion rules adaptively through the decomposed coefficients. However, in the aforementioned methods [5], [20], CNN is just used to obtain the final weight map, where the useful deep feature maps are ignored. Besides, the number of CNN layers are relatively small and they are incapable of performing the feature extraction sufficiently. To further resolve this issue, Li et al. [19] uses the pretrained network ResNet50 [23] to explore deep feature maps extraction, and then the feature maps are processed by zero-phase component analysis (ZCA) and softmax operation to obtain the final weight maps. Finally, the fused image is reconstructed with a weighted-averaging rule according to the final weight maps.

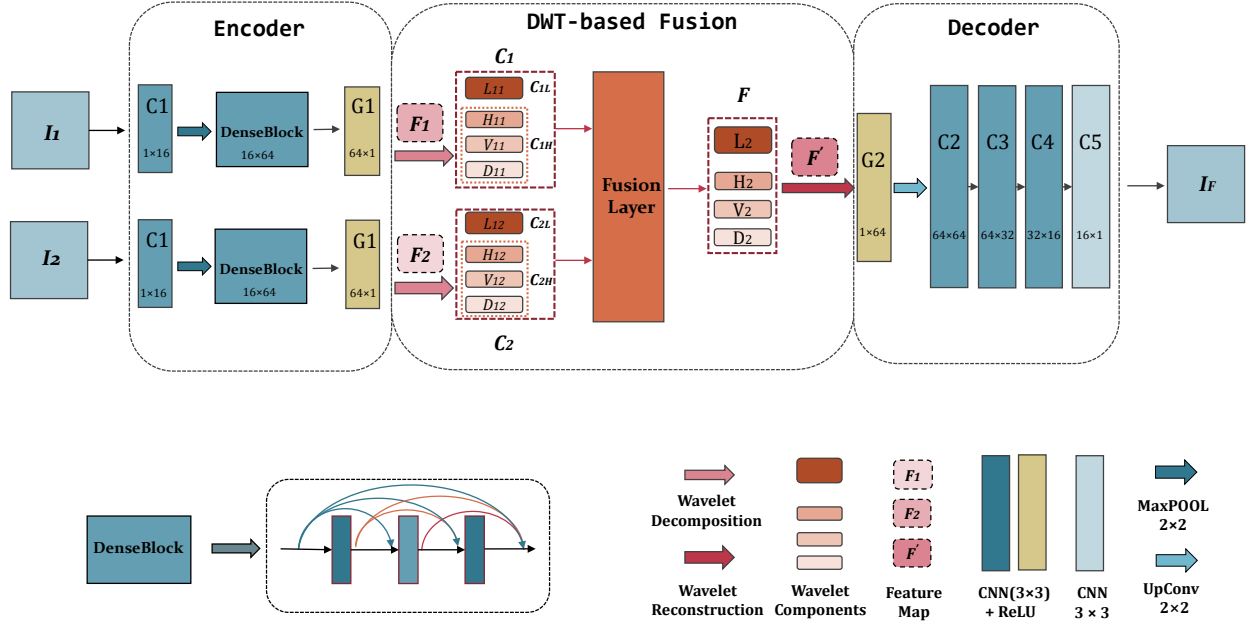


Fig. 2. Architecture of the proposed WaveFuse image fusion network. The feature maps learned by the encoder from the input images are processed by multi-scale discrete wavelet transform, and finally the fused feature maps are utilized to the fused image reconstruction by the decoder.

2) *Encoder-Decoder Based Methods*: DeepFuse [16] is the first encoder-decoder based image fusion architecture and it is designed for multi-exposure image fusion. The encoding network is trained to extract useful feature maps from the source images, and then an appropriate fusion rule is applied to fuse the feature maps. Finally, the decoding network is employed to reconstruct the fused image. However, in Deepfuse [16], the network just fuses the features extracted from the last layer of the encoder, losing a lot of useful information in the middle layers. To further resolve this issue, DenseFuse [17] used dense blocks in the encoder and a new $l1$ -Norm fusion rule to fuse the feature maps. Considering that DenseFuse only works on a single scale, Song et al. [4] proposed a multi-scale medical image fusion framework, MSDNet. In MSDNet, three different filters are applied to extract feature maps in the encoding layer. Both [4] and [17] are trained by using a mixed loss function consisting of the modified structural similarity metric (MS-SSIM) and the mean square error (MSE). To achieve gradient transformation and suppress noise interference, VIF-Net [24] was proposed based on a robust mixed loss function including MS-SSIM and the total variation (TV). However, the deep features are not leveraged effectively in these methods, because they just fuse the feature maps with simple weighted average or direct concatenation. In order to better utilize feature maps, [25] attempted to perform feature map fusion using CNN, where the extracted feature maps are first concatenated, and then processed by a convolutional layer. Nevertheless, the feature maps fusion is still performed in the spatial domain, with a large amount of detail information of features not fully utilized [20]. In our method, we introduced DWT to the feature fusion, where the feature maps are first transformed to wavelet domain and then adaptive fusion rules are used to make the best use of the transformed feature maps.

3) *GAN Based Methods*: Due to availability and effectiveness of conditional GAN [26], the FusionGAN [21] was proposed by Ma *et al.* to fuse infrared and visible images using a generative adversarial network. The fused image generated by the generator is expected to capture more details existing in the visible image by applying the discriminator to distinguish differences between them. However, the training of GAN-based network is a demanding task due to the trade-off between generator and discriminator.

III. PROPOSED METHOD

The proposed method, WaveFuse, is a novel network by introducing DWT and adding more convolutional layers based on the backbone network, DenseFuse [17]. To enable effective local information utilization, we introduce DWT-based decomposition and reconstruction module and utilize the region-based fusion rules in the fusion part. The architecture of the proposed network is shown in Fig. 2.

A. Network Architecture

WaveFuse is a typical encoder-decoder architecture, consisting of three components: an encoder, a DWT-based fusion part and a decoder. The symbol like 1×16 in encoder and decoder means the input channel of CNN is 1 and the output channel of CNN is 16. As shown in Fig. 2, the inputs of the network are spatially aligned source images I_k , where $k = 1, 2$ is used to index the images. Feature maps F_k are obtained by extracting features from the input source images I_k through the encoder. The feature maps F_k are first transformed into the wavelet domain, and an adaptive fusion rule is used to obtain the fused feature map F' . Finally, the fused feature map is input into the decoder to obtain the final fused image I_F .

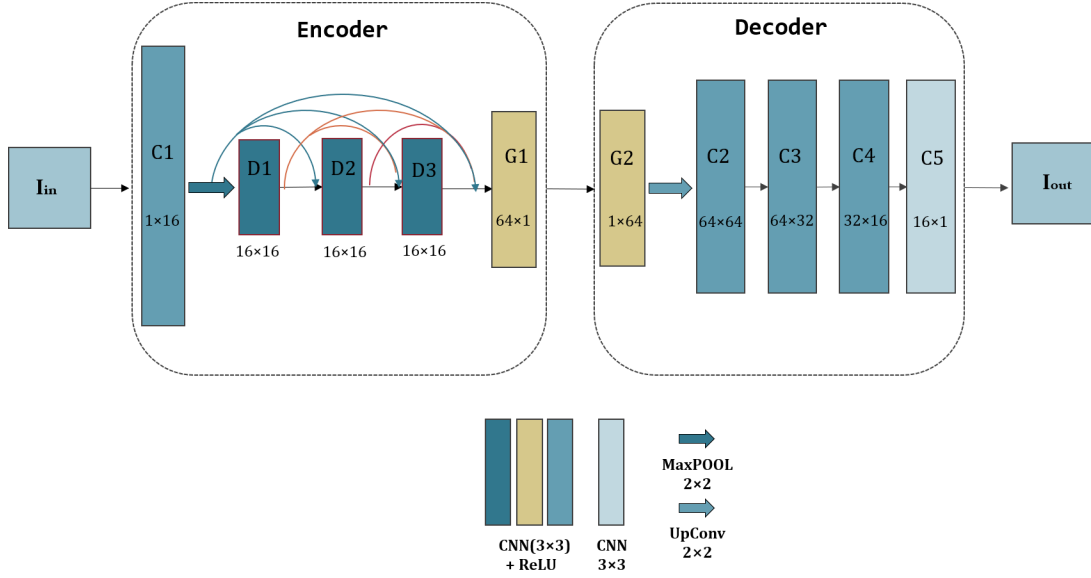


Fig. 3. The architecture of the trained network. The objective of the training phase is to obtain an encoder-decoder network that tries to make the input and the output image as similar as possible.

The encoder is composed of a convolutional layer C1, a maxpooling layer, a DenseBlock [27] module and a convolutional feature generator G1. The kernel size of both C1 and G1 are all 3×3 . C1 is used to initially extract features from the image, and G1 is used to generate the feature maps for the wavelet decomposition.

In the DWT-based fusion part, to take 1 layer decomposition for example, the feature maps F_k are decomposed to different wavelet components C_k , including one low-frequency component C_{kL} , namely L_{1k} and three high-frequency components C_{kH} : horizontal component H_{1k} , vertical component V_{1k} and diagonal component D_{1k} , respectively. Different fusion rules are employed for different components to obtain the fused wavelet components F , where the low-frequency component L_2 is obtained from the fusion of L_{11} and L_{12} , and the high-frequency components H_2 , V_2 and D_2 are obtained from the fusion of H_{1k} , V_{1k} and D_{1k} , respectively. Finally, the fused low-frequency component and high-frequency components are integrated by wavelet reconstruction to obtain the final fused feature map F' .

The decoder is mainly composed of the deconvolution layer G2 and convolutional layers C2-C5. The fused feature map is first enlarged through G2 and upsampled by the deconvolutional layer. Then, the fused image is finally reconstructed by C2-C5.

B. Loss Function

The loss function L used to train the encoder and the decoder in WaveFuse is a weighted combination of pixel loss L_p and structural similarity loss L_{ssim} with a weight λ , where λ is assigned as 1000 according to [17]. The loss function L , pixel loss L_p and structural similarity loss L_{ssim} are defined as follows:

$$L = L_p + \lambda L_{ssim}, \quad (1)$$

$$L_p = \|I_{out} - I_{in}\|_2, \quad (2)$$

$$L_{ssim} = 1 - SSIM(I_{out}, I_{in}), \quad (3)$$

where I_{in} and I_{out} represent the input image to the encoder and the output image of the decoder, respectively. The structural similarity (SSIM) is a widely used perceptual image quality metric, which combines the three components of luminance, structure and contrast to comprehensively measure image quality [28].

C. Training

In the field of image fusion, it is a challenging task to learn effective fusion network and rules under end-to-end supervision for the lack of golden standard fused image. Therefore, the main objective of our training process is to ensure that the decoder can reconstruct the image from the feature maps encoded by the encoder with the lowest image quality loss, and then we can leverage the feature maps obtained by the encoder for fusion. Additionally, the DWT-based fusion part in Fig. 2 is discarded in training because no trainable parameters are involved in it. The trained model is illustrated in Fig. 3. We trained our network using COCO [29] containing 70,000 images, and all of them were resized to 256×256 and transformed to gray images. The batch size and epochs were set as 64 and 50, respectively. Learning rate was 1×10^{-4} . The proposed method was implemented on Pytorch 1.1.0 with Adam as the optimizer and a NVIDIA GTX 2080 Ti GPU for training. In our practical training process, we found that using comparatively small dataset, containing 300-700 images chosen randomly from COCO, still achieved a comparable fusion quality. The parameters for small dataset

are as follows: learning rate was set as 1×10^{-4} , and the batch size and epochs were 4 and 500, respectively.

D. Fusion Rule

The selection of fusion rules largely determines the quality of fused images [5]. Existing image fusion algorithms based on deep learning usually calculate the sum of the feature maps directly, leaving the information of feature maps not fully mined.

In our method, two complementary fusion rules based on DWT are adopted for wavelet components C_k transformed by feature maps F_k , including adaptive rule based on regional energy [30] and *II-Norm* rule [17], and the fused wavelet components are denoted as F_r and F_{l1} , respectively. In adaptive rule based on regional energy, different fusion rules are employed for different frequency components, that is, the low-frequency components C_{kL} adopts an adaptive weighted averaging algorithm based on regional energy, and for the high-frequency components C_{kH} , the one with larger variance between C_{1H} and C_{2H} will be selected as the fused high-frequency components. Additionally, to preserve more structural information and make our fused image more natural, we apply *II-Norm* rule [17] to our fusion part, where both low and high frequency components are fused by the same rule to obtain global and general fused wavelet components. Therefore, in the fusion part, the extracted feature maps F_k are processed by two abovementioned rules, and the final fused wavelet components F is calculated by the weighted averaging of F_r and F_{l1} , which is defined as follows:

$$F(m, n) = \omega_r F_r(m, n) + \omega_{l1} F_{l1}(m, n), \quad (4)$$

s.t. $\omega_r + \omega_{l1} = 1$,

where (m, n) denotes the corresponding position in C_k and F , and ω_r will be set as different values for different scenarios to achieve the optimal fusion performance. In our experiments, ω_r is set as 0.6 for infrared and visible image, 1 for multi-focus image and 0.4 for multi-modal medical image. In the following part, these two fusion rules will be introduced in detail.

We first introduce adaptive rule based on regional energy. As is mentioned above, different fusion rules are adopted for low-frequency and high-frequency components. Therefore, F_r includes two parts, the fused low-frequency component F_{rL} and the fused high-frequency components F_{rH} . For high-frequency components, we employ a rule of maximizing variance, where F_{rH} is obtained from the one with larger variance between C_{1H} and C_{2H} , and the details are introduced in [31]. For low-frequency components, we employ a rule of weighted average based on regional energy, which is introduced as follows:

We use $E_l(m, n)$ ($l = 1, 2$) to represent the energy in the 3×3 region centered at (m, n) , which is defined as follows:

$$E_l(m, n) = \sum_{m'=-1}^1 \sum_{n'=-1}^1 \omega(m+m', n+n') [C_l(m+m', n+n')]^2, \quad (5)$$

$$\omega = \frac{1}{16} \begin{bmatrix} 1 & 2 & 1 \\ 2 & 4 & 2 \\ 1 & 2 & 1 \end{bmatrix}, \quad (5a)$$

where ω means weighted coefficients and C_l represents wavelet frequency components. The matching degree M_{12} of C_{1L} and C_{2L} is defined as follows:

$$M_{12}(m, n) = \frac{2 \sum_{m'=-1}^1 \sum_{n'=-1}^1 \omega(\Delta m, \Delta n) C_1(\Delta m, \Delta n) C_2(\Delta m, \Delta n)}{E_1(m, n) + E_2(m, n)}, \quad (6)$$

where $\Delta m = m + m'$, $\Delta n = n + n'$. A threshold T on $M_{12}(m, n)$ is used to determine how the pixel at (m, n) is fused, and T is set as 0.8 in our network. When $M_{12}(m, n)$ is smaller than T , it means that the energy of the two feature maps in this local region is greatly discriminative. In this way, the central pixel of the region with the larger energy value will be selected as the central pixel of the feature map F_{rL} , which is calculated as follows:

$$\begin{cases} F_{rL}(m, n) = C_1(m, n), & \text{if } E_1(m, n) \geq E_2(m, n). \\ F_{rL}(m, n) = C_2(m, n), & \text{if } E_1(m, n) < E_2(m, n). \end{cases} \quad (7)$$

On the contrary, when $M_{12}(m, n)$ is greater than or equal to T , it means the two feature maps have similar energy in this local region. Consequently, a weighted fusion rule [30] is used to determine the central pixel of the feature map F_{rL} , and it is defined as follows:

$$\begin{cases} F_{rL}(m, n) = \omega_{max}(m, n) C_1(m, n) + \omega_{min}(m, n) C_2(m, n), & \text{if } E_1(m, n) \geq E_2(m, n). \\ F_{rL}(m, n) = \omega_{min}(m, n) C_1(m, n) + \omega_{max}(m, n) C_2(m, n), & \text{if } E_1(m, n) < E_2(m, n). \end{cases} \quad (8)$$

$$\omega_{max}(m, n) = \frac{1}{2} - \frac{1}{2} \left[\frac{1 - M_{12}(m, n)}{1 - T} \right], \quad (8a)$$

$$\omega_{min}(m, n) = 1 - \omega_{max}(m, n). \quad (8b)$$

Then, the feature map F_{l1} generated by *II-Norm* rule is denoted as follows:

$$F_{l1}(m, n) = \sum_{l=1}^2 \omega_l(m, n) \times C_l(m, n), \quad (9)$$

$$\omega_l(m, n) = \frac{\hat{C}_l(m, n)}{\sum_{\xi=1}^2 \hat{C}_\xi(m, n)}, \quad (9a)$$

$$\hat{C}_l(m, n) = \frac{\sum_{a=-r}^r \sum_{b=-r}^r \|C_l(m+a, n+b)\|_1}{(2r+1)^2}, \quad (9b)$$

where r means the block size and r is set as 1 according to [17].

TABLE I

THE AVERAGE VALUES OF FUSION QUALITY METRICS FOR SIX FUSED IMAGES OF THREE DIFFERENT SCENARIOS. RED ONES ARE THE BEST RESULTS, AND WAVEFUSE RESULTS AMONG TOP TWO ARE MARKED ORANGE. FOR ALL METRICS, LARGER IS BETTER.

IR_VIS	EN	MI	Qabf	MS_SSIM	STD	AVG	EIN	VIF
DWT	6.3189	12.6377	0.4289	0.8830	22.9205	3.7287	35.8938	0.3679
CBF	*	*	*	*	*	*	*	*
ConvSR	*	*	*	*	*	*	*	*
WLS	6.7412	13.4824	0.4755	0.9294	33.8465	4.5559	44.0795	0.7463
ResZCA	6.4447	12.8893	0.2387	0.6323	27.1435	2.2178	22.7138	0.2899
FusionGAN	6.5888	13.1775	0.1519	0.5477	28.3121	1.9382	20.1227	0.2826
DenseFuse	6.5140	13.0280	0.4338	0.8474	29.4581	2.5841	25.8742	0.4141
WaveFuse	6.8580	13.7161	0.3754	0.8723	35.5306	3.6939	38.4883	0.6339
WaveFuse_3_db1	6.9152	13.8304	0.3876	0.8884	36.2466	3.9474	41.3366	0.7155
Multi-focus	EN	MI	Qabf	MS_SSIM	STD	AVG	EIN	VIF
DWT	7.2438	14.4877	0.4998	0.9547	44.4301	4.9644	51.9155	0.6918
CBF	7.2550	14.5100	0.6774	0.9886	45.3357	5.8665	61.0520	0.8483
ConvSR	7.2737	14.5474	0.6957	0.9867	46.2913	5.9747	63.1097	0.8794
WLS	7.2786	14.5571	0.6631	0.9839	45.6133	5.8128	60.5427	0.8681
DenseFuse	7.2142	14.4285	0.5958	0.9680	43.9375	4.3209	45.9510	0.7235
WaveFuse	7.3561	14.7123	0.5196	0.9594	48.1359	6.5495	69.8810	0.8380
WaveFuse_3_db1	7.3830	14.7660	0.5176	0.9556	48.9388	6.6945	71.3553	0.8363
Medical	EN	MI	Qabf	MS_SSIM	STD	AVG	EIN	VIF
DWT	5.3748	10.7497	0.4827	0.8789	53.4287	6.2316	63.1409	0.5942
CBF	*	*	*	*	*	*	*	*
ConvSR	*	*	*	*	*	*	*	*
WLS	5.5099	11.0197	0.5771	0.9226	63.5586	6.9586	71.3395	0.8305
DenseFuse	5.3300	10.6599	0.6055	0.8742	63.7758	5.4067	57.0015	0.6988
WaveFuse	5.5883	11.1767	0.5119	0.8854	69.6581	6.8353	71.3563	0.8057
WaveFuse_3_db1	5.5755	11.1509	0.5127	0.8870	70.1196	7.3028	75.3542	0.7986

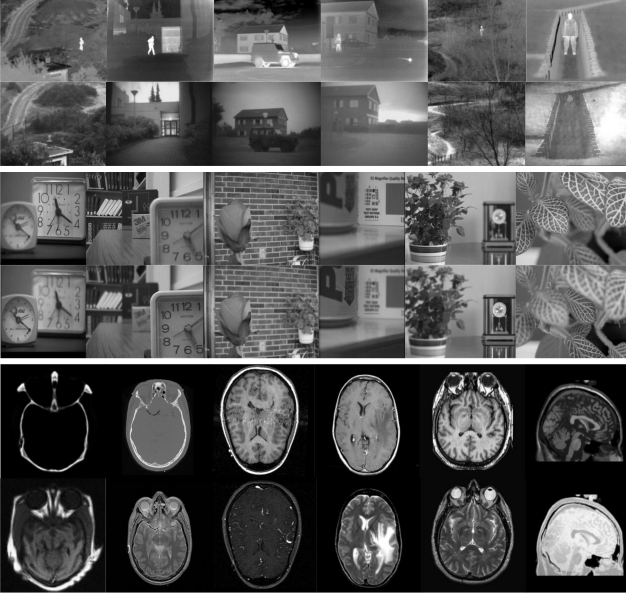


Fig. 4. Six pairs of source images in each fusion task. From top to bottom are infrared and visible images, multi-focus images and multi-modal medical images, respectively.

IV. EXPERIMENTAL RESULTS AND ANALYSIS

In this section, to validate the effectiveness and generalization of our WaveFuse, we first compare it with several state-of-the-art methods on three fusion tasks, including infrared and

visible, multi-focus and multi-modal medical image fusion. The source images of three scenarios are shown in Fig. 4. There are six pairs of images in each scenario, and all the images are available online [32]. For quantitative comparison, we use eight metrics to evaluate the fusion results. Then, we evaluate the fusion performance of the proposed method trained with small datasets. Finally, we also conduct the fine-tuning experiments on wavelet parameters for the further improvement of fusion performance. In our following experiments *A* and *B*, the wavelet decomposition layer is set as two and *sym2* is chosen as wavelet base.

A. Compared Methods and Quantitative Metrics

WaveFuse is compared against seven representative peer methods including discrete wavelet transform (DWT) [6], cross bilateral filter method (CBF) [33], convolutional sparse representation (ConvSR) [22], weighted least square optimization-based method (WLS) [34], ResNet50 and zero-phase component analysis fusion framework (ResZCA) [19], GAN-based fusion algorithm (FusionGAN) [21] and DenseFuse [17]. All the seven comparative methods were implemented based on public available codes, where the parameters were set according to the original papers. Note that, ResZCA and FusionGAN are designed for infrared and visible images, so they are only compared in the infrared and visible image fusion task.

Due to the diversity of image fusion scenario, it turns out to be difficult to evaluate the quality of the fused images

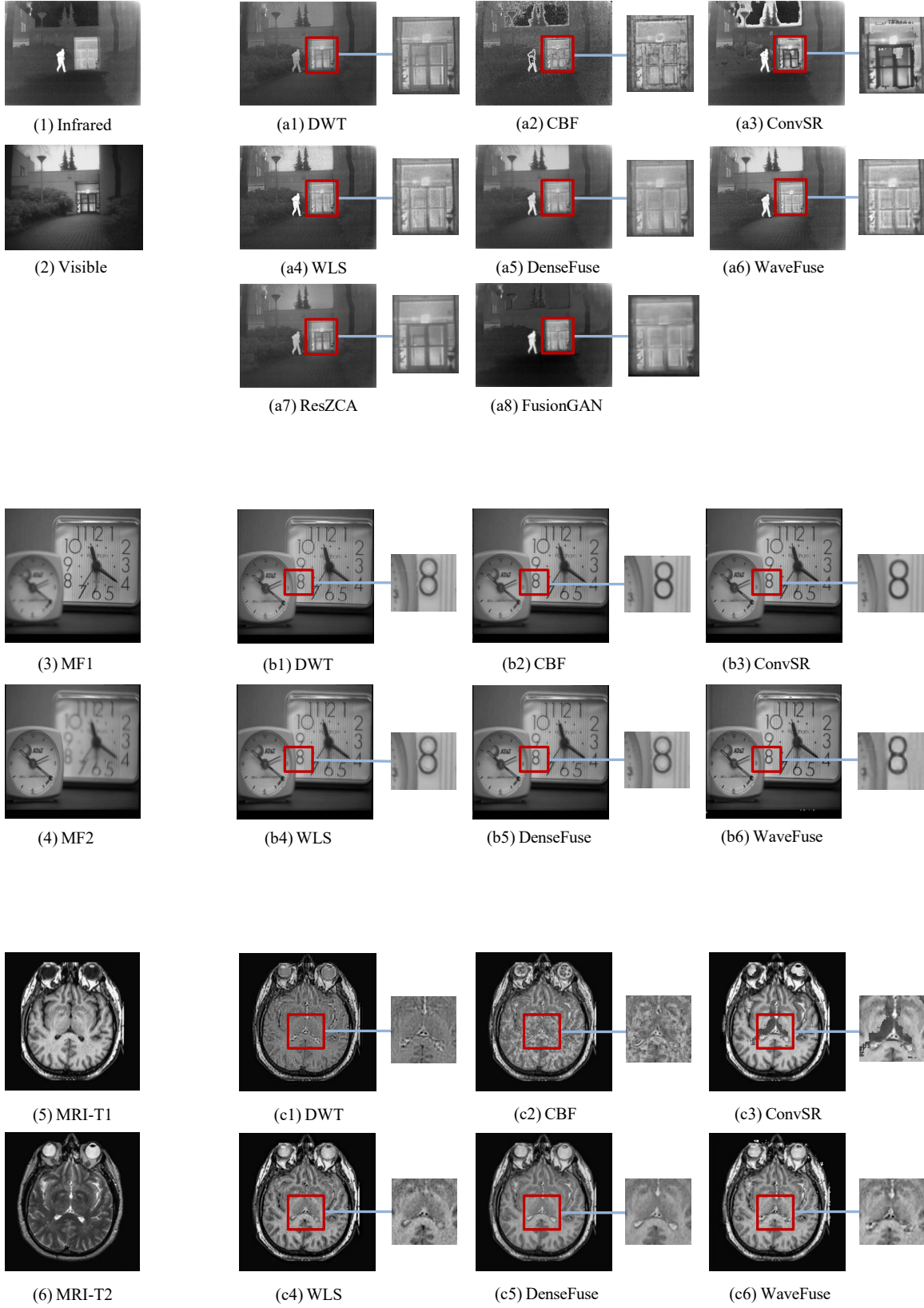


Fig. 5. Fusion results by different methods. (1)-(6) are Infrared, Visible, different focus (MF1, MF2), MRI-T1 and MRI-T2 source images, respectively. (a1)-(a8) are infrared and visible fused images obtained by eight different fusion methods. (b1)-(b6) are multi-focus fused images, and (c1)-(c6) are multi-modal medical fused images.

objectively and comprehensively with a unified framework of metrics. The commonly used evaluation methods can be classified into two categories: subjective evaluation and objective evaluation. Subjective evaluation is susceptible to human factors, such as eyesight, subjective preference and individual emotion. Furthermore, no prominent difference among the fusion results can be observed in most cases based on subjective evaluation. In contrast, objective evaluation is a relatively accurate and quantitative method on the basis of mathematical and statistical models. In our experiments, we adopted the following objective evaluation metrics: information entropy (EN) [35], mutual information (MI) [36], Qabf [37], multiscale structural similarity (MS-SSIM) [38], visual information fidelity (VIF) [39], standard deviation (STD) [40], average gradient (AVG) and edge intensity (EIN) [41].

EN and MI are used to measure the informative richness of the fused image. The larger the EN and MI is, the greater the richness of information is contained in the image and the higher quality of the fused image achieves. Qabf is a novel objective non-reference quality evaluation index of the fused image. It uses local metrics to estimate the performance of significant information in the fused image. Higher Qabf value means better quality of the fused image [37]. MS-SSIM is an extension of SSIM [28] and it is more consistent with the visual perception of human visual system. VIF is proposed to follow human visual system to compute the distortion between two random variables. STD is based on statistical characteristics. Larger STD indicates higher gray dispersion of an image, leading to higher information richness. AVG and EIN are based on gradients, reflecting the difference in the details of the image and the texture changes, respectively. The larger the eight quality metrics are, the better the fusion results will be.

B. Comparison to Other Methods

1) *Subjective Evaluation*: Examples of the original image pairs and the fusion results obtained by each comparative method for the three scenarios are shown in Fig. 5. The red boxes mark the region of interest that should be focused in the fusion results.

Infrared/Visible Image Fusion: Visible images can capture more detail information compared to infrared images. However, the interested objects can not be easily observed in visible image especially when it is under low contrast circumstance and the light is insufficient. Infrared images can provide thermal radiation information, making it easy to detect the salient object even in complex background. Thus, the fused image can provide more complementary information. Fig. 5 (a1-a8) show fusion results of infrared and visible images with the eight comparison methods. CBF and ConvSR exhibit significant artifacts and unclear salient objects. Focused on the "door" in red boxes, the results in DWT and DenseFuse weaken the contrast. We can see that, WaveFuse preserves more details in high contrast and brightness.

Multi-focus Image Fusion: The multi-focus image fusion aims to reconstruct a fully focused image from partly focused images of the same scene. From Fig. 5 (b1-b6), we can observe

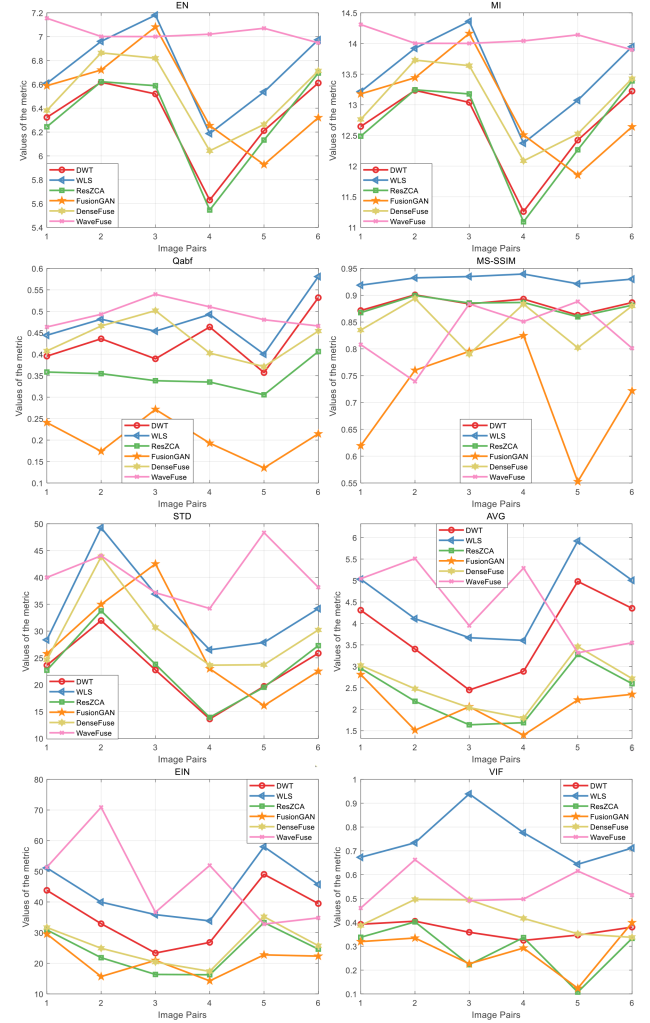


Fig. 6. Quantitative comparison of our WaveFuse for infrared and visible image fusion with 7 state-of-the-art methods.

that all the compared methods perform well. Focused on the number "8" in the red boxes, CBF and WaveFuse outperform other methods with high resolution.

Multi-modal Medical Image Fusion: Multi-modal medical image fusion can offer more accurate and effective information for biomedical research and clinical applications. Better multi-modal medical fused image should provide combined features sufficiently and preserve both significant textural features. As shown in Fig. 5 (c1-c6), ConvSR shows obvious artifacts in the whole image. DWT and CBF fail to preserve the crucial features of the source images. DenseFuse shows better visual results than the above-mentioned methods. However, DenseFuse still weakens the details and brightness. Information-rich fused images can be obtained by WLS. In contrast, our method preserves the details and edge information of both source images, which is more in line with the perception characteristics of the human vision compared to other fusion methods.

2) *Objective Evaluation*: The main purpose of image fusion is to increase the richness of image information, so EN and MI are the most important evaluation metrics in the three fusion tasks. Given the differences among different scenarios,

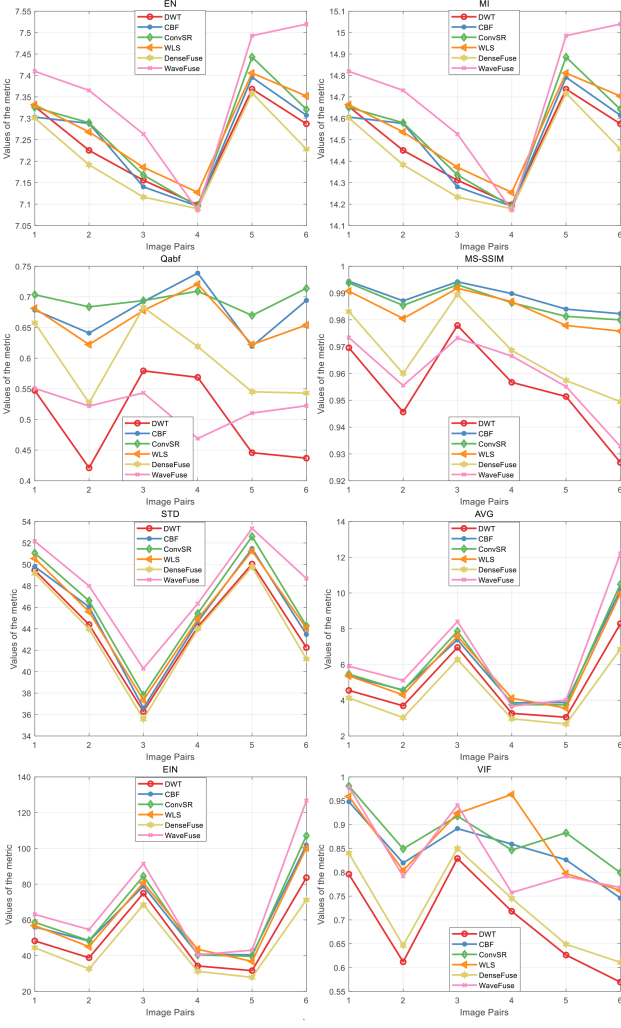


Fig. 7. Quantitative comparison of our WaveFuse for multi-focus image fusion with 5 state-of-the-art methods.

the emphasis on evaluation metrics of various fusion tasks should be placed differently. For infrared and visible images, SSIM and VIF are decisive metrics to ensure the information retention and visual information integrity of each band. In multi-focus image fusion, detail information should be saved, so STD and EIN are more important. In multi-modal medical image fusion, STD and AVG should be considered in priority. Besides, from Fig. 5 (a2-a3) and (b2-b3), we can observe that the fusion results of CBF and ConvSR in infrared and visible images and multi-modal medical images contain poor visual effects owing to considerable artificial noise, and in this case their objective quality metrics will not be calculated for the quantitative evaluation.

Table I shows the average values of the fusion quality metrics among three different fusion tasks by different fusion methods. In the infrared and visible image fusion, our method obtains the highest metrics in EN, MI and STD, and ranks the second in MS-SSIM, AVG, EIN and VIF. In multi-focus image fusion, our method ranks first in EN, MI, STD, AVG, EIN, and ranks the fourth in VIF. In multi-modal medical image fusion, our method ranks first in EN, MI, STD and EIN, and ranks

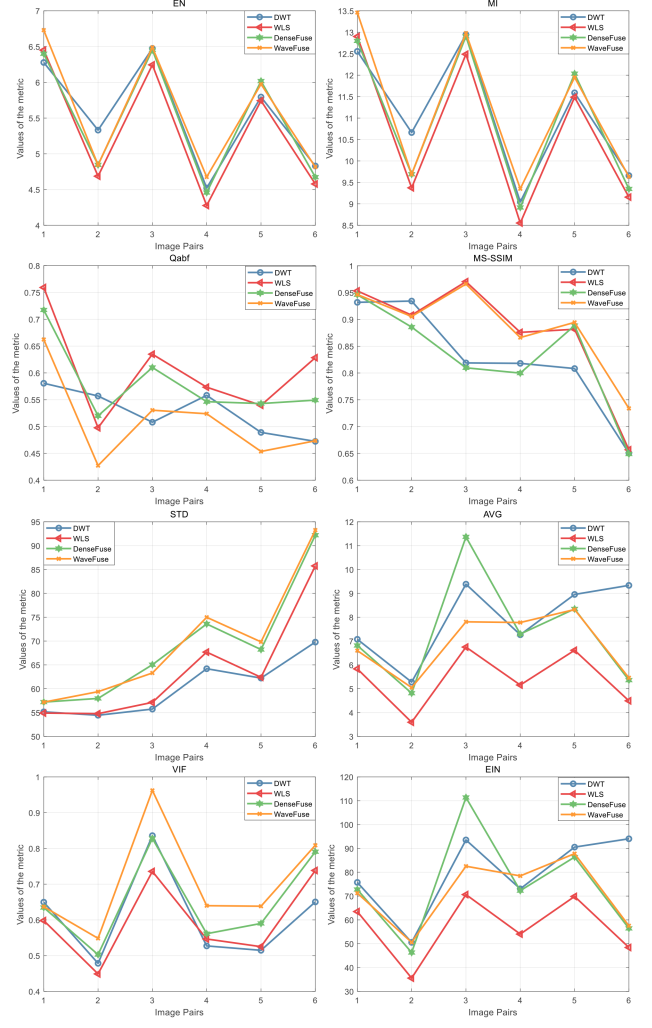


Fig. 8. Quantitative comparison of our WaveFuse for multi-modal medical image fusion with 5 state-of-the-art methods.

second in MS-SSIM, AVG and VIF, and ranks third in Qabf. Furthermore, from the value of the last row among three image fusion task in Table I, better fusion performance are obtained through wavelet parameters fine-tuning, and more details will be discussed in section D. Figure 6-8 shows the curve of fusion quality metrics obtained in three kinds of fused images. In Fig. 6-8, the results show the consistency of our fusion performance among six pairs of images, which demonstrate the robust and universality of our method. Overall, our proposed method achieves the best performance.

C. Comparison of Using Different Training Dataset

In order to further demonstrate the effectiveness and robustness of our network, we conducted experiments on another three different training minisets: MINI1-MINI3, each of which contains 300, 500 and 700 images respectively chosen randomly from COCO, and the fusion results are shown in Fig. 9 and Table II. We compared the fusion results of WaveFuse on COCO and MINI1-MINI3. The same three sets of images and ω_{RE} values were chosen for testing process. The fusion performance was compared and analyzed by the averaged

TABLE II
QUANTITATIVE COMPARISON OF WAVEFUSE WITH DIFFERENT TRAINING DATASETS. THE METRICS OF MINI ARE OBTAINED BY THE AVERAGE OF MINI1-MINI3. RED ONES ARE THE BEST METRICS. FOR ALL METRICS, LARGER IS BETTER.

Application	Dataset	EN	MI	Qabf	MS_SSIM	STD	AVG	EIN	VIF
IR_VIS	COCO	6.8583	13.7167	0.3755	0.8722	35.5311	3.6948	38.4966	0.6338
	MINI	6.8751	13.7502	0.3688	0.8677	35.8324	3.7616	39.2384	0.6576
Multi-focus	COCO	7.3561	14.7123	0.5199	0.9594	48.1370	6.5520	69.9019	0.8383
	MINI	7.3672	14.7345	0.5174	0.9541	48.4257	6.9271	73.8873	0.8686
Medical	COCO	5.5881	11.1761	0.5119	0.8854	69.6581	6.8352	71.3558	0.8057
	MINI	5.6629	11.3258	0.5056	0.8529	70.6554	7.8938	81.2461	0.7995

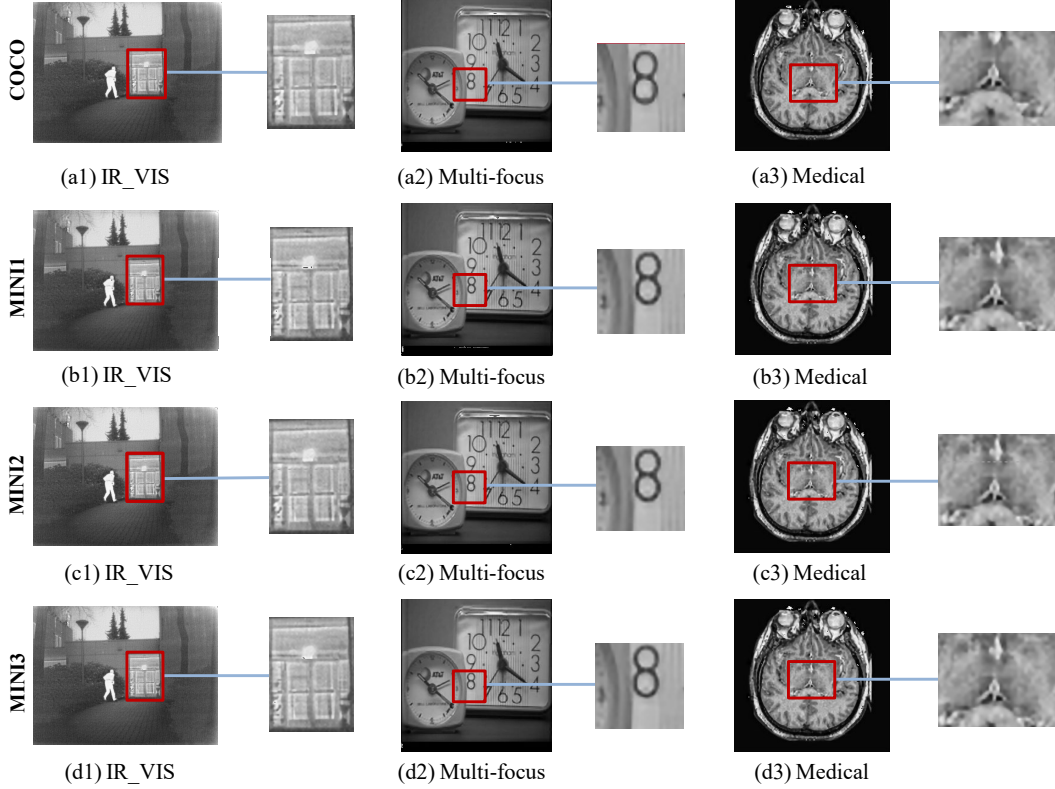


Fig. 9. Fusion results with different training datasets in WaveFuse.

fusion quality metrics. From the fusion results in Fig. 9, no obvious visual difference can be found among the fused images in WaveFuse when different training sets are chosen. Then objective metrics are employed to evaluate the fusion performance.

TABLE III
COMPARISON OF TRAINING EFFICIENCY IN WAVEFUSE WITH DIFFERENT DATASETS, AND THE METRICS OF MINI ARE OBTAINED BY THE AVERAGE OF MINI1-MINI3

	Time(h)	GPU(MB)
COCO	7.78	8517
MINI	0.76	1681

The fusion metrics of WaveFuse trained with the different training datasets are shown in Table II. In WaveFuse, higher performance is even achieved by training on minisets. Furthermore, from Table III, we can observe that WaveFuse

is trained on minisets within one hour, where the GPU memory utilization is just 1681 MB, so it can be trained with lower computational cost. Accordingly, we can learn that our proposed network is robust both to the size of the training dataset and to the selection of training images.

D. Comparison of Using Different Wavelet Decomposition Layers and Bases

In wavelet transform, the number of decomposition layers and the selection of different wavelet bases could exert great impacts on the effectiveness of wavelet transform. In the following experiments with COCO dataset, different wavelet decomposition layers and bases are selected for further optimization on our proposed method.

1) *Experiments on Different Wavelet Decomposition Layers*: We chose decomposition layers from 1 to 4, and wavelet base was set as *sym2* [42] in this experiment. From Table IV and Fig. 10, we can clearly see that the higher fusion metrics,

higher brightness and contrast of the fused images are obtained with the increase of decomposition layers. However, when the decomposition layer is set as 3, fusion results exhibit a little artificial noise in visible and infrared images, and when the decomposition layer is set as 4, except for multi-focus images, other fused images contain obvious noise. From the above analysis, the number of decomposition layer is not the more the better, and the evaluation of fused images should be considered both subjectively and objectively.

TABLE IV

QUANTITATIVE COMPARISON WITH DIFFERENT WAVELET DECOMPOSITION LAYERS IN WAVEFUSE. THE FUSION QUALITY METRICS FOR SIX FUSED IMAGES OF THREE DIFFERENT SCENARIOS ARE OBTAINED BY AVERAGE OPERATION. RED ONES ARE THE BEST RESULTS. FOR ALL METRICS, LARGER IS BETTER.

Application	Layer	EN	MI	Qabf	MS_SSIM	STD	AVG	EIN	VIF
IR_VIS	1	6.8251	13.6501	0.3716	0.8494	35.2559	3.5373	36.5797	0.5941
	2	6.8583	13.7167	0.3755	0.8722	35.5311	3.6948	38.4966	0.6338
	3	6.8994	13.7988	0.3829	0.8928	35.9602	3.7396	39.0690	0.6789
	4	6.9580	13.9159	0.3843	0.9023	36.7579	3.7598	39.2986	0.7237
Multi-focus	1	7.3349	14.6699	0.4809	0.9494	47.4765	6.3098	66.8584	0.7533
	2	7.3561	14.7123	0.5199	0.9594	48.1370	6.5520	69.9019	0.8383
	3	7.3676	14.7353	0.5296	0.9599	48.6419	6.6343	70.7985	0.8688
	4	7.3767	14.7534	0.5295	0.9587	48.9999	6.6592	71.0260	0.8712
Medical	1	5.5585	11.1170	0.5277	0.8805	69.6862	6.5261	68.4686	0.8081
	2	5.5881	11.1761	0.5119	0.8854	69.6581	6.8352	71.3558	0.8057
	3	5.6743	11.3487	0.5038	0.8812	70.0103	7.2669	75.2111	0.8009
	4	5.7541	11.5081	0.5005	0.8731	70.3898	7.6128	78.2182	0.7820

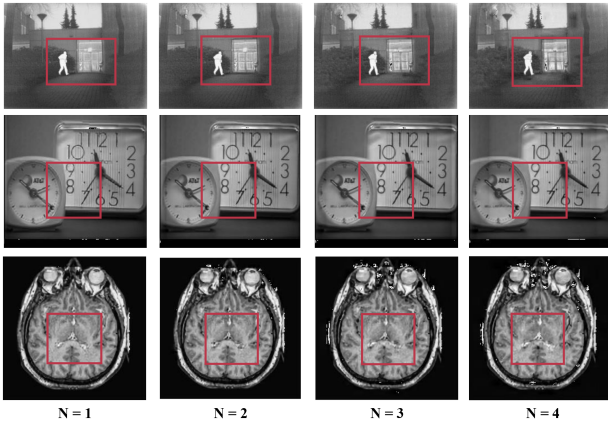


Fig. 10. Fusion results obtained by our WaveFuse with different wavelet decomposition layers.

2) *Experiments on Different Wavelet Bases*: For the comparison of using different wavelet bases, we set the decomposition layer as 3, and four bases including *sym2* [42], *sym3* [42], *db1* [43] and *rbio6.8* [44] were chosen. From a subjective point of view in Fig. 11, we find it difficult to distinguish which wavelet base achieves better fusion performance. Combined with the objective evaluation metrics in Table. V, the fusion quality of wavelet base *db1* is the highest in the three image fusion scenarios. Through the above two experiments, we can further improve our proposed method by selecting the appropriate number of decomposition layers and wavelet bases, providing a new direction for the follow-up improvement of our method.

V. CONCLUSIONS

In this paper, we propose a novel image fusion method through the combination of a multi-scale discrete wavelet

TABLE V

QUANTITATIVE COMPARISON WITH DIFFERENT WAVELET BASES IN WAVEFUSE. THE FUSION QUALITY METRICS FOR SIX FUSED IMAGES OF THREE DIFFERENT SCENARIOS ARE OBTAINED BY AVERAGE OPERATION. RED ONES ARE THE BEST RESULTS. FOR ALL METRICS, LARGER IS BETTER.

Application	Method	EN	MI	Qabf	MS_SSIM	STD	AVG	EIN	VIF
IR_VIS	<i>sym2</i>	6.8995	13.7990	0.3833	0.8931	35.9582	3.7392	39.0663	0.6791
	<i>sym3</i>	6.8950	13.7901	0.3831	0.8935	35.9461	3.6904	38.5472	0.6833
	<i>db1</i>	6.9152	13.8304	0.3876	0.8884	36.2466	3.9474	41.3366	0.7155
	<i>rbio6.8</i>	6.8989	13.7977	0.3812	0.8887	35.9574	3.6857	38.4857	0.6747
Multi-focus	<i>sym2</i>	7.3676	14.7353	0.5296	0.9599	48.6419	6.6343	70.7985	0.8688
	<i>sym3</i>	7.3700	14.7401	0.5299	0.9575	48.6571	6.6658	71.1048	0.8726
	<i>db1</i>	7.3830	14.7660	0.5176	0.9556	48.9388	6.6945	71.3553	0.8363
	<i>rbio6.8</i>	7.3609	14.7218	0.5328	0.9624	48.5020	6.5911	70.2980	0.8756
Medical	<i>sym2</i>	5.6743	11.3487	0.5038	0.8812	70.0103	7.2669	75.2111	0.8009
	<i>sym3</i>	5.7093	11.4185	0.4998	0.8828	69.9106	7.1585	74.0353	0.7939
	<i>db1</i>	5.5755	11.1509	0.5127	0.8870	70.1196	7.3028	75.3542	0.7986
	<i>rbio6.8</i>	5.6831	11.3662	0.4810	0.8604	69.8820	7.2228	74.5406	0.7656

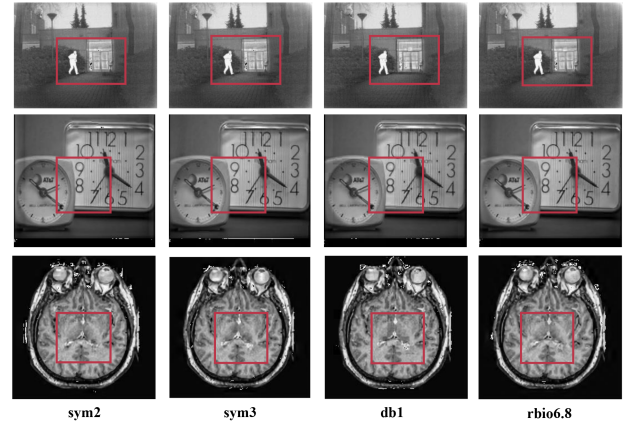


Fig. 11. Fusion results obtained by our WaveFuse with different wavelet bases.

transform based on regional energy and deep learning. To our best knowledge, this is the first time that a conventional technique is integrated for feature maps fusion in the pipeline of deep learning based image fusion methods, and we think there are still a lot of possibilities to explore in this direction.

Our network consists of three parts: an encoder, a DWT-based fusion part and a decoder. The features of the input image are extracted by the encoder, then we use the adaptive fusion rule at the fusion layer to obtain the fused features, and finally reconstruct the fused image through the decoder. Compared with existing fusion algorithms, our proposed method achieves better performance. Additionally, our network has strong universality and can be applied to various image fusion scenarios. At the same time, our network can be trained in smaller datasets to obtain the comparable fusion results trained in large datasets with shorter training time and higher efficiency, alleviating the dependence on large datasets. Extensive experiments on different wavelet decomposition layers and bases demonstrate the possibility of further improvement of our method.

REFERENCES

- [1] A. A. Goshtasby and S. Nikolov, "Image fusion: advances in the state of the art," *Information fusion*, vol. 2, no. 8, pp. 114–118, 2007.
- [2] S. Li, X. Kang, L. Fang, J. Hu, and H. Yin, "Pixel-level image fusion: A survey of the state of the art," *information Fusion*, vol. 33, pp. 100–112, 2017.

- [3] Y. Liu, X. Chen, Z. Wang, Z. J. Wang, R. K. Ward, and X. Wang, "Deep learning for pixel-level image fusion: Recent advances and future prospects," *Information Fusion*, vol. 42, pp. 158–173, 2018.
- [4] X. Song, X.-J. Wu, and H. Li, "Msdnet for medical image fusion," in *International Conference on Image and Graphics*. Springer, 2019, pp. 278–288.
- [5] Y. Liu, X. Chen, H. Peng, and Z. Wang, "Multi-focus image fusion with a deep convolutional neural network," *Information Fusion*, vol. 36, pp. 191–207, 2017.
- [6] H. Li, B. Manjunath, and S. K. Mitra, "Multisensor image fusion using the wavelet transform," *Graphical models and image processing*, vol. 57, no. 3, pp. 235–245, 1995.
- [7] J.-L. Starck, E. J. Candès, and D. L. Donoho, "The curvelet transform for image denoising," *IEEE Transactions on image processing*, vol. 11, no. 6, pp. 670–684, 2002.
- [8] A. L. Da Cunha, J. Zhou, and M. N. Do, "The nonsubsampling contourlet transform: theory, design, and applications," *IEEE transactions on image processing*, vol. 15, no. 10, pp. 3089–3101, 2006.
- [9] W. Wang and F. Chang, "A multi-focus image fusion method based on laplacian pyramid," *JCP*, vol. 6, no. 12, pp. 2559–2566, 2011.
- [10] Q. Zhang and B.-I. Guo, "Multifocus image fusion using the nonsub-sampled contourlet transform," *Signal processing*, vol. 89, no. 7, pp. 1334–1346, 2009.
- [11] S. Li, J. T. Kwok, and Y. Wang, "Combination of images with diverse focuses using the spatial frequency," *Information Fusion*, vol. 2, no. 3, pp. 169–176, 2001.
- [12] S. Li and X. Kang, "Fast multi-exposure image fusion with median filter and recursive filter," *IEEE Transactions on Consumer Electronics*, vol. 58, no. 2, pp. 626–632, 2012.
- [13] A. Garcia-Garcia, S. Orts-Escobedo, S. Oprea, V. Villena-Martinez, P. Martinez-Gonzalez, and J. Garcia-Rodriguez, "A survey on deep learning techniques for image and video semantic segmentation," *Applied Soft Computing*, vol. 70, pp. 41–65, 2018.
- [14] W. Rawat and Z. Wang, "Deep convolutional neural networks for image classification: A comprehensive review," *Neural computation*, vol. 29, no. 9, pp. 2352–2449, 2017.
- [15] Z.-Q. Zhao, P. Zheng, S.-t. Xu, and X. Wu, "Object detection with deep learning: A review," *IEEE transactions on neural networks and learning systems*, vol. 30, no. 11, pp. 3212–3232, 2019.
- [16] K. R. Prabhakar, V. S. Srikanth, and R. V. Babu, "Deepfuse: A deep unsupervised approach for exposure fusion with extreme exposure image pairs," in *ICCV*, 2017, pp. 4724–4732.
- [17] H. Li and X.-J. Wu, "Densefuse: A fusion approach to infrared and visible images," *IEEE Transactions on Image Processing*, vol. 28, no. 5, pp. 2614–2623, 2018.
- [18] C. Du and S. Gao, "Image segmentation-based multi-focus image fusion through multi-scale convolutional neural network," *IEEE access*, vol. 5, pp. 15 750–15 761, 2017.
- [19] H. Li, X.-J. Wu, and T. S. Durrani, "Infrared and visible image fusion with resnet and zero-phase component analysis," *Infrared Physics & Technology*, vol. 102, p. 103039, 2019.
- [20] Y. Liu, X. Chen, J. Cheng, and H. Peng, "A medical image fusion method based on convolutional neural networks," in *2017 20th International Conference on Information Fusion (Fusion)*. IEEE, 2017, pp. 1–7.
- [21] J. Ma, W. Yu, P. Liang, C. Li, and J. Jiang, "FusionGAN: A generative adversarial network for infrared and visible image fusion," *Information Fusion*, vol. 48, pp. 11–26, 2019.
- [22] Y. Liu, X. Chen, R. K. Ward, and Z. J. Wang, "Image fusion with convolutional sparse representation," *IEEE signal processing letters*, vol. 23, no. 12, pp. 1882–1886, 2016.
- [23] K. He, X. Zhang, S. Ren, and J. Sun, "Deep residual learning for image recognition," in *Proceedings of the IEEE conference on computer vision and pattern recognition*, 2016, pp. 770–778.
- [24] R. Hou, D. Zhou, R. Nie, D. Liu, L. Xiong, Y. Guo, and C. Yu, "Vif-net: an unsupervised framework for infrared and visible image fusion," *IEEE Transactions on Computational Imaging*, vol. 6, pp. 640–651, 2020.
- [25] H. Jung, Y. Kim, H. Jang, N. Ha, and K. Sohn, "Unsupervised deep image fusion with structure tensor representations," *IEEE Transactions on Image Processing*, vol. 29, pp. 3845–3858, 2020.
- [26] M. Mirza and S. Osindero, "Conditional generative adversarial nets," *arXiv preprint arXiv:1411.1784*, 2014.
- [27] G. Huang, Z. Liu, L. Van Der Maaten, and K. Q. Weinberger, "Densely connected convolutional networks," in *Proceedings of the IEEE conference on computer vision and pattern recognition*, 2017, pp. 4700–4708.
- [28] Z. Wang, A. C. Bovik, H. R. Sheikh, and E. P. Simoncelli, "Image quality assessment: from error visibility to structural similarity," *IEEE transactions on image processing*, vol. 13, no. 4, pp. 600–612, 2004.
- [29] T.-Y. Lin, M. Maire, S. Belongie, J. Hays, P. Perona, D. Ramanan, P. Dollár, and C. L. Zitnick, "Microsoft coco: Common objects in context," in *European conference on computer vision*. Springer, 2014, pp. 740–755.
- [30] S. Xiao-hua, G.-s. Yang, and H.-l. Zhang, "Improved on the approach of image fusion based on region-energy," *Journal of Projectiles, Rockets, Missiles and Guidance*, vol. 4, 2006.
- [31] B. Zhang, "Study on image fusion based on different fusion rules of wavelet transform," in *2010 3rd International Conference on Advanced Computer Theory and Engineering (ICACTE)*, vol. 3. IEEE, 2010, pp. V3–649.
- [32] S. Liu, Song, and Wang, "Testing dataset," <https://github.com/moveERIC/WaveFuse>.
- [33] B. S. Kumar, "Image fusion based on pixel significance using cross bilateral filter," *Signal, image and video processing*, vol. 9, no. 5, pp. 1193–1204, 2015.
- [34] J. Ma, Z. Zhou, B. Wang, and H. Zong, "Infrared and visible image fusion based on visual saliency map and weighted least square optimization," *Infrared Physics & Technology*, vol. 82, pp. 8–17, 2017.
- [35] Y.-J. Rao, "In-fibre bragg grating sensors," *Measurement science and technology*, vol. 8, no. 4, p. 355, 1997.
- [36] M. Hossny, S. Nahavandi, and D. Creighton, "Comments on information measure for performance of image fusion," *Electronics letters*, vol. 44, no. 18, pp. 1066–1067, 2008.
- [37] C. Xydeas and V. Petrovic, "Objective image fusion performance measure," *Electronics letters*, vol. 36, no. 4, pp. 308–309, 2000.
- [38] K. Ma, K. Zeng, and Z. Wang, "Perceptual quality assessment for multi-exposure image fusion," *IEEE Transactions on Image Processing*, vol. 24, no. 11, pp. 3345–3356, 2015.
- [39] H. R. Sheikh and A. C. Bovik, "Image information and visual quality," *IEEE Transactions on image processing*, vol. 15, no. 2, pp. 430–444, 2006.
- [40] J. W. Roberts, J. A. van Aardt, and F. B. Ahmed, "Assessment of image fusion procedures using entropy, image quality, and multispectral classification," *Journal of Applied Remote Sensing*, vol. 2, no. 1, p. 023522, 2008.
- [41] B. Rajalingam and R. Priya, "Hybrid multimodality medical image fusion technique for feature enhancement in medical diagnosis," *International Journal of Engineering Science Invention*, vol. 2, no. Special issue, pp. 52–60, 2018.
- [42] R. Singh, R. E. Vasquez, and R. Singh, "Comparison of daubechies, coiflet, and symlet for edge detection," in *Visual Information Processing VI*, vol. 3074. International Society for Optics and Photonics, 1997, pp. 151–159.
- [43] J.-M. Lina and M. Mayrand, "Complex daubechies wavelets," *Applied and Computational Harmonic Analysis*, vol. 2, no. 3, pp. 219–229, 1995.
- [44] W. Sweldens, "Lifting scheme: a new philosophy in biorthogonal wavelet constructions," in *Wavelet applications in signal and image processing III*, vol. 2569. International Society for Optics and Photonics, 1995, pp. 68–79.